Non-RPA behavior of the valence plasmon in SrTi$_{1-x}$Nb$_x$O$_3$

Caitlin S. Kengle,[1,2] Samantha I. Rubeck,[1,2] Melinda Rak,[1,2] Jin Chen,[1,2] Faren Hoveyda [1,2] Simon Bettler,[1,2] Ali Husain [1,2] Matteo Mitrano [1,2,*] Alexander Edelman [3,4] Peter Littlewood,[3,4] Tai-Chang Chiang [1,2] Fahad Mahmood,[1,2] and Peter Abbamonte [1,2,†]

[1]*Department of Physics, University of Illinois, Urbana, Illinois 61801, USA*
[2]*Materials Research Laboratory, University of Illinois, Urbana, Illinois 61801, USA*
[3]*James Franck Institute, 929 East 57th Street, Chicago, Illinois 60637, USA*
[4]*Department of Physics, The University of Chicago, 5720 South Ellis Avenue, Chicago, Illinois 60637, USA*

Doped SrTi$_{1-x}$Nb$_x$O$_3$ is a dilute polaronic metal that exhibits superconductivity and a mid-infrared optical response suggesting parallels with copper oxides. A peculiar feature of SrTi$_{1-x}$Nb$_x$O$_3$ is that its plasma frequency, ω_p, is highly temperature dependent, increasing by more than a factor of 2 when the system is cooled from 300 to 100 K [F. Gervais *et al.*, Phys. Rev. B **47**, 8187 (1993); D. M. Eagles *et al.*, Phys. Rev. B **54**, 22 (1996); C. Z. Bi *et al.*, J. Phys.: Condens. Matter **18**, 2553 (2006)]. There is still no generally accepted explanation for this dramatic shift. Here, we present momentum-resolved electron energy-loss spectroscopy measurements of SrTi$_{1-x}$Nb$_x$O$_3$ at nonzero momentum, q. We also calculate the collective excitations of SrTi$_{1-x}$Nb$_x$O$_3$ using the random phase approximation (RPA), to assess whether the behavior of the collective modes conforms to established explanations. We find that the plasmon energy and linewidth are momentum independent, in contrast to RPA predictions, and that its shift with temperature takes place everywhere in the Brillouin zone, from $q = 0$ to the zone boundary, $q = 0.5$ reciprocal lattice units. We also find that the phonon frequencies do not shift with q in the expected way, suggesting the screening properties of the material deviate significantly from RPA predictions. We conclude that a radically different starting point, perhaps based on lattice anharmonicity, may be needed to explain the collective charge excitations of SrTi$_{1-x}$Nb$_x$O$_3$.

I. INTRODUCTION

The cubic perovskite SrTiO$_3$ is a quantum paraelectric that, when doped with niobium or oxygen, becomes a polaronic metal with dilute superconductivity [1–5]. Doped SrTiO$_3$ exhibits evidence for quantum criticality, a peculiar mid-infrared (IR) optical response, and violates the Mott-Ioffe-Regel limit (i.e., exhibiting so-called "bad metal" behavior [6]), suggesting close parallels with the copper-oxide superconductors [2,7–9]. Understanding SrTiO$_3$ and its doped variants therefore remains of perennial importance.

A perplexing property of doped SrTiO$_3$ is that its plasma frequency, ω_p, is temperature dependent. In SrTi$_{1-x}$Nb$_x$O$_3$, ω_p increases by a factor of ~ 2 as the material is cooled from 300 to 100 K [10–12]. This change is normally interpreted as a changing effective mass of the conduction electrons, m^*, which appears to be supported by some transport experiments [13,14]. However, the reason why m^* should change so much is unclear. A leading explanation was the mixed polaron theory proposed by Eagles [11], which postulates that SrTi$_{1-x}$Nb$_x$O$_3$ contains both large and small polarons whose relative population changes with temperature, resulting in an apparent change in m^* [11]. However, subsequent optics

studies found this picture to be inconsistent with the total spectral weight in the Drude response and the size of the coupling constant, $\alpha \sim 2$, which rules out the presence of small polarons [15,16]. The origin of the temperature-dependent plasma frequency in doped SrTiO$_3$ therefore remains unexplained.

The frequency and line shape of the valence plasmon are direct measures of the density and scattering rate of quasiparticles in a conductor [17]. The seeming absence of even a qualitative explanation for the plasmon in SrTi$_{1-x}$Nb$_x$O$_3$ is a serious problem for the overall understanding of the low-energy physics of this material. There is therefore a great need for new experimental characterizations of the collective charge excitations in this material.

The random phase approximation (RPA) is an established technique for computing the behavior of plasmons and other collective modes in materials. Previous RPA calculations on doped SrTiO$_3$ [18] made concrete predictions for the behavior of the dielectric response, $\epsilon(q, \omega)$. The main findings were that the plasma frequency, $\omega_p(q)$, should be proportional to $\sqrt{n}$ at $q = 0$, n being the density of doped electrons, and disperse like q^2 at small q. The plasmon lifetime should be infinite until it enters the particle-hole continuum, after which it should decay with increasing q due to Landau damping.

In RPA, longitudinal optical (LO) phonons should be highly influenced by the presence of the plasmon, in two distinct ways. First, the existence of doped electrons leads to screening, which should shift the LO phonon frequencies. On
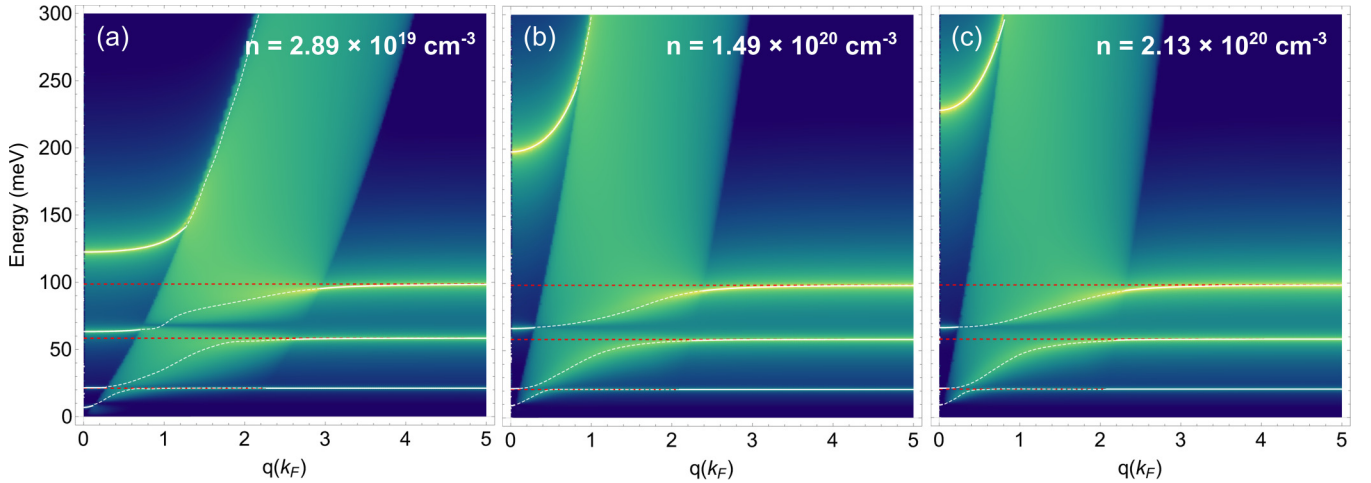
FIG. 1. RPA calculations of plasmon and phonon modes in $SrTi_{1-x}Nb_xO_3$ with carrier concentrations (a) 2.89×10^{19} cm^{-3} ($\sim$0.2%), (b) 1.49×10^{20} cm^{-3} ($\sim$1%), and (c) 2.13×10^{20} cm^{-3} ($\sim$1.4%). The features are broadened by $10^{-3}E_F \sim 10$ meV for visibility. Dashed red lines indicate the unscreened LO phonon frequencies of 21, 58, and 93 meV. Dashed white lines are guides to the eye of the LO phonons, interpolated when they become undefined inside the continuum.

the other hand, the presence of a distinct plasmon mode will shift the phonons through level repulsion effects. For coupling constants appropriate for doped $SrTi_{1-x}Nb_xO_3$, increasing n should lead to an overall increase in the phonon frequencies at $q = 0$ [18].

For sufficiently large momenta, $q \gg k_F$, where k_F is the Fermi momentum, the plasmon in RPA should be fully damped into the particle-hole continuum and the phonons should relax to the unscreened frequencies observed in insulating $SrTiO_3$ [18]. As described below in Sec. "RPA calculations," we confirmed these predictions using parameters appropriate for doped $SrTi_{1-x}Nb_xO_3$. The overall behavior is summarized in Fig. 1.

In order to understand the origin and nature of the plasmon in $SrTi_{1-x}Nb_xO_3$, a measure of the finite-q dielectric response is needed. Here we report an energy- and momentum-resolved study of the dynamic charge response of the normal state of niobium-doped $SrTiO_3$ using momentum-resolved electron energy-loss spectroscopy (M-EELS) to provide additional insight into the behavior of this unusual plasmon and investigate to what extent $SrTi_{1-x}Nb_xO_3$ adheres to the expectations of RPA.

We find that the plasmon in $SrTi_{1-x}Nb_xO_3$, identified as such by its doping dependence, width, and temperature dependence, does not disperse as q^2. The plasmon is present across the entire Brillouin zone and has a q-independent width. The longitudinal optical phonons do not shift with q, and remain at their large-q, unscreened frequencies everywhere in the Brillouin zone. The shift of the phonon frequencies with doping at $q = 0$ is significantly smaller than predicted by RPA. From these results it is clear that a more sophisticated, beyond-RPA approach may be needed to explain the behavior of the plasmon and phonons in $SrTi_{1-x}Nb_xO_3$.

II. RPA CALCULATIONS

We begin by calculating the RPA response at carrier concentrations similar to those addressed in experiment. While

multiple bands of electrons can be partly filled depending on the doping, for simplicity we consider the single-band Hamiltonian,

$$H = \sum_{\mathbf{k}} \xi_{\mathbf{k}} c_{\mathbf{k}}^\dagger c_{\mathbf{k}} + \sum_{s\mathbf{k}} \Omega_s b_{s\mathbf{k}}^\dagger b_{s\mathbf{k}} + \sum_{s\mathbf{q}} g_{s\mathbf{q}} \rho_{\mathbf{q}} (b_{s\mathbf{q}} + b_{s-\mathbf{q}}^\dagger)$$
$$+ \sum_{\mathbf{q}} V_c(\mathbf{q}) \rho_{\mathbf{q}} \rho_{-\mathbf{q}}, \qquad (1)$$

where an electron in a single band with dispersion $\xi_{\mathbf{k}} = \mathbf{k}^2/2m^* - \mu$ is annihilated by $c_{\mathbf{k}}$. The density is controlled by the chemical potential μ. We use an average band mass $m^* = 0.8$ [16]. The electrons are coupled to Einstein LO phonon modes indexed by s, annihilated by $b_{s\mathbf{k}}$. Following [16] we use $\Omega_1 = 21.1$ meV, $\Omega_2 = 58.4$ meV, and $\Omega_3 = 98.7$ meV, consistent with the phonon frequencies observed in our experimental discussion. The electron-phonon interaction is of the long-range Fröhlich type, so that the phonon displacements couple to the electron density $\rho_{\mathbf{q}} = \sum_{\mathbf{k}} c_{\mathbf{k}}^\dagger c_{\mathbf{k}+\mathbf{q}}$. The coupling constant can be written $g_{s\mathbf{q}}^2 = \Omega_s \gamma_s V_c(q)$, where $V_c(q) = 4\pi e^2/\epsilon_\infty q^2$ is the Coulomb coupling. $\gamma_1 = 0.002$, $\gamma_2 = 0.09$, and $\gamma_3 = 0.4$ are the dimensionless parameters which give the measured values of the Fröhlich coupling constant, α of the LO phonon modes, respectively. In these units, the condition $\sum_s \gamma_s \to 0.5$ would imply a diverging static dielectric constant $\epsilon_0 \to \infty$ as the lowest transverse-optical (TO) frequency softens to zero, and thus the onset of ferroelectricity.

We approximate the total dielectric function to leading order by

$$\epsilon(\omega, q) = \epsilon_\infty - V_c(q)\Pi_{ph}(\omega) - V_c(q)\Pi_{RPA}(\omega, q), \qquad (2)$$

where $\epsilon_\infty = 5.4$ [16] is the optical dielectric constant, $\Pi_{ph}(\omega)$ is the polarizability of the phonons, and $\Pi_{RPA}(\omega, q)$ is the polarizability of the electron gas within the random phase approximation. In terms of the effective electron-electron

interaction,

$$\epsilon^{-1}(\omega, q) = \frac{\epsilon_\infty^{-1} V_c^{-1}(q)[V_c(q) + V_{ph}(\omega, q)]}{1 - \Pi_{RPA}(\omega, q)[V_c(q) + V_{ph}(\omega, q)]}, \quad (3)$$

where $V_{ph}(\omega, q) = V_c(q) \sum_s \gamma_s \frac{2\Omega_s}{\omega^2 - \Omega_s^2}$ is the phonon-mediated electron-electron interaction. This result may be obtained by integrating out the (quadratic) phonons in Eq. (1) and performing a diagrammatic summation of the possible combinations of direct Coulomb and phonon-mediated interactions with electron-hole polarization bubbles as in [19].

We plot $\text{Im}\,\epsilon^{-1}(\omega + i\delta, q)$ for the nominal experimental concentrations of $n = 2.89 \times 10^{19}$ cm^{-3} [$k_F = 0.0949$ Å$^{-1} = 0.0590$ reciprocal lattice units (r.l.u.)], $n = 1.49 \times 10^{20}$ cm^{-3} ($k_F = 0.164$ Å$^{-1} = 0.102$ r.l.u.), and $n = 2.13 \times 10^{20}$ cm^{-3} ($k_F = 0.185$ Å$^{-1} = 0.115$ r.l.u.) in Figs. 1(a), 1(b), and 1(c), respectively. The plot is broadened by $\delta = 10^{-3} E_F$, comparable to the experimental resolution, for visibility. The momentum axes are plotted in units of k_F [20].

In all cases the behaviors at low and high momenta are demarcated by the electron-hole continuum, bounded by the lines $\omega_\pm(q) = q^2/2m \pm v_F q$. At high momenta, the spectrum consists of peaks at the bare LO phonon frequencies. In contrast, at low momenta there is substantial hybridization between the plasmon of the electron gas and the phonons, with most of the oscillator strength in the uppermost, plasmonlike mode, which eventually disperses into the continuum.

The results in Fig. 1 are consistent with the conclusions of Ref. [18]; the plasmon should disperse as q^2 from its $q = 0$ plasma frequency, ω_p, until it decays into the electron-hole continuum at $\omega_\pm(q) = q^2/2m \pm v_F q$. As seen in Fig. 1, the plasmon width is resolution limited at $q = 0$ and increases as a result of Landau damping. With increased carrier concentration, there is a $\sqrt{n}$ increase in the $q = 0$ plasma frequency.

In all panels of Fig. 1, at small q, the optical phonons in the system are weak in intensity and shifted down in frequency relative to their high-q counterparts due to level repulsion with the plasmon. All of the longitudinal optical phonons are strongly hybridized at low q, with the highest frequency mode having the most significant coupling. The combination of level repulsion and screening shifts the phonon frequencies to higher value as doping is increased and as q is increased until $q \geqslant k_F$. At $q \geqslant k_F$, the system can no longer support a collective electronic excitation and the phonons shift to their unscreened frequencies, shown in Fig. 1.

Note that there is no notion of temperature in the RPA model, so the previously measured temperature dependence of the plasmon [10,12] is not captured, nor is any potential temperature dependence of the LO phonons.

III. M-EELS EXPERIMENT

Momentum-resolved EELS (M-EELS) experiments were performed with 50 eV electrons using a setup described previously [21–23]. The M-EELS cross section is given by

$$\frac{\partial^2 \sigma}{\partial \Omega \partial E} = \sigma_0 M^2(q) S_s(q, \omega), \quad (4)$$

where $S_s(q, \omega)$ is the surface density-density correlation function of the surface of a material, σ_0 is a factor
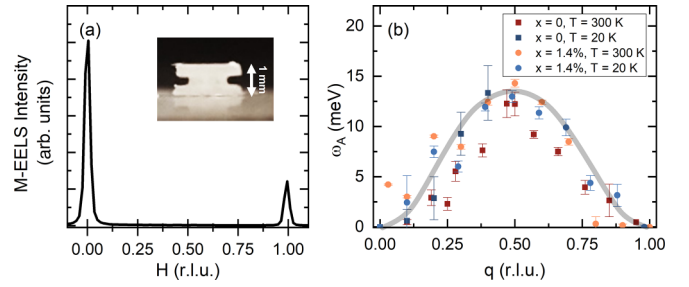

FIG. 2. Room temperature characterization of SrTi$_{1-x}$Nb$_x$O$_3$ sample surfaces. (a) Elastic M-EELS diffraction scans along $(H, 0)$ showing the crystallinity of samples studied. Inset: notched $x = 0\%$ sample before fracturing. (b) Dispersion of the peak of the acoustic phonon at $T = 300$ K and $T = 20$ K of an $x = 0\%$ sample and an $x = 1.4\%$ sample. The line is a guide to the eye.

depending on the beam energy and sample surface reflectivity, and $M(q) = 4\pi e^2/[q^2 + (k_i^z + k_s^z)^2]$ is the Coulomb matrix element [21,22]. $S_s(q, \omega)$ is related to the dynamic charge response of a semi-infinite system, $\chi_s''(q, \omega)$, by the fluctuation-dissipation theorem [21,22]:

$$S_s(q, \omega) = -\frac{1}{\pi}\left[\frac{1}{1 - e^{-k_B T/\hbar\omega}}\right]\chi_s''(q, \omega). \quad (5)$$

For nonzero values of q, we obtained the correlation function $S_s(q, \omega)$ from our M-EELS data by dividing σ_0 and $M^2(q)$ from the raw spectra. At the momenta of interest here, this division resulted in a negligible correction to the shape of the spectra. For $q = 0$, $M^2(q)$ is a very rapidly varying function of ω, which departs from the analytic form [24]. For this reason, at $q = 0$ we show the raw data. All spectra were normalized to the total spectral weight.

M-EELS measurements were performed on samples of SrTi$_{1-x}$Nb$_x$O$_3$ with $x = 0$, 0.2%, 1%, and 1.4%. Hall measurements of the $x = 0.2\%$, 1%, and 1.4% samples showed them to be electron doped with carrier densities $(2.89 \pm 0.26) \times 10^{19}$, $(1.49 \pm 0.14) \times 10^{20}$, and $(2.13 \pm 0.07) \times 10^{20}$ cm^{-3}, respectively. Hall measurements could not be performed on the undoped SrTiO$_3$ samples, as they were too insulating. That said, previous reports suggest that a conducting, two-dimensional electron gas can be created on the surface of undoped SrTiO$_3$ by exposure to intense UV light in ultrahigh vacuum [25], which creates surface oxygen vacancies. Exposure to our 50-eV electron beam in pressures $\mathcal{O}(10^{-10}$ Torr) might also lead to a conducting surface layer, meaning there is some possibility our undoped sample may behave, in M-EELS measurements, as if it is slightly metallic. Further, the carrier concentrations of the doped samples may be higher than the nominal values measured by Hall effect. We will keep this possibility in mind as we interpret the results of our measurements.

Surfaces were prepared by notching the sides of the samples [Fig. 2(a), inset] and fracturing in ultrahigh vacuum along a (0,0,1) surface normal. All measurements were performed with the momentum transfer vector, q, oriented parallel to the (1,0) surface reciprocal lattice direction. Momenta in this paper will be stated in reciprocal lattice units, e.g., a momentum $q = 0.5$ r.l.u. corresponds to the Brillouin zone boundary. The
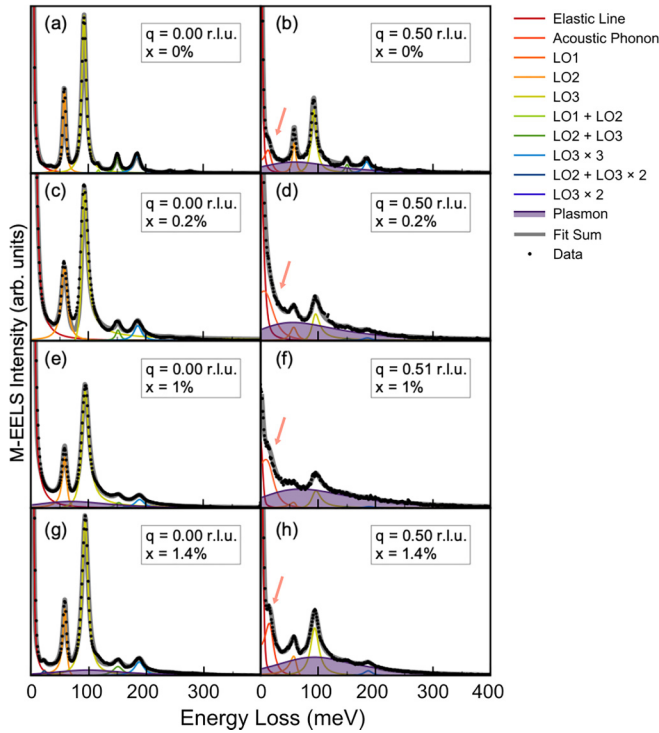
FIG. 3. M-EELS spectra at $T = 300$ K for $x = 0\%$ at (a) $q = 0$ and (b) $q = 0.50$ r.l.u., $x = 0.2\%$ at (c) $q = 0$ and (d) $q = 0.50$ r.l.u., $x = 1\%$ at (e) $q = 0$ and (f) $q = 0.51$ r.l.u., and $x = 1.4\%$ at (g) $q = 0$ and (h) $q = 0.50$ r.l.u. Solid lines represent fits to the phonons and the elastic line. The shaded areas represent fits to the plasmon. The orange arrows in the right-hand column point to the acoustic phonon shoulder on the elastic line.

fractured surfaces are conchoidal [26] and sufficiently crystallographically pristine to provide momentum conservation in M-EELS experiments, demonstrated by resolution-limited (0,0) and (1,0) Bragg peaks [Fig. 2(a)] and a dispersing acoustic phonon [Fig. 2(b)]. This illustrates that momentum is conserved, i.e., our M-EELS measurements should be sensitive to the dispersion of other collective modes.

IV. RESULTS

The M-EELS data for the sample with the highest doping, $x = 1.4\%$, in which all the relevant excitations are visible, are shown in Fig. 3. Figures 3(g) and 3(h) show spectra for $q = 0$ and 0.5 r.l.u., respectively, at $T = 300$ K for this sample. The acoustic phonon in Fig. 2(b) is visible in panel (h) of Fig. 3 as a shoulder on the elastic line. This phonon reaches a maximum energy of 14 meV at $q = 0.5$ r.l.u., consistent with previous neutron-scattering studies [27–29].

Three LO phonons are also visible at $q = 0$ [Fig. 3(g)] with energies 33, 59, and 94 meV, which we designate LO1, LO2, and LO3, respectively. The LO3 phonon has been identified as a Fuchs-Kliewer (FK) mode polarized perpendicular to the surface, which scatters strongly in this geometry [30,31]. Additional peaks at integer multiples of the LO1, LO2, and LO3 phonon frequencies correspond to overtones due to multiple scattering of the probe electron, also consistent with previous reports [30,31].

Figures 3(g) and 3(h) also show the valence plasmon, which appears as a broad background beneath the phonons (this assignment is confirmed by its temperature dependence, discussed further below). Its energy at $q = 0$ is consistent with IR optics experiments [10,12]. But its width is significantly broader than RPA [Fig. 1(c)], which predicts a plasmon with an infinite lifetime. This width discrepancy represents a significant departure from RPA, and demonstrates the presence of significant decay mechanisms beyond the usual Landau damping.

The plasmon has the same energy and width at $q = 0.5$ as it does at $q = 0$ [Figs. 3(g) and 3(h)]. It fails to exhibit the q^2 dispersion predicted by RPA (Fig. 1). It may be that the dispersion is simply not visible because the width of the plasmon is so large. However, $q = 0.5$ r.l.u. is well beyond the predicted onset of the particle-hole continuum, yet the plasmon remains as a resolvable feature. In fact, the only observable difference between the plasmon at these two momenta is its intensity, which is significantly higher at $q = 0.5$ than at $q = 0$.

The LO phonons also do not conform with RPA predictions. The LO phonons have the same energy at $q = 0.5$ as at $q = 0$, in contrast to RPA predictions that they should shift from a lower, screened energy at $q \sim 0$ to a higher, bare frequency at $q \gg k_F$ [Fig. 1(c)].

To quantify these observations, we fit our data using a pseudo-Voigt function for the elastic line, and Fano functions for the LO phonons. A single Drude function was found to provide the best fit to the plasmon. For the acoustic phonon, which, depending on the cleave and the value of q, can appear as a distinct peak or a shoulder on the elastic line, we used the general expression for dynamics of a scalar order parameter in time-dependent Landau theory [32],

$$f(A, \mu, \tau, \omega) = \frac{A\omega}{\omega^2 + (\mu\omega^2 - \tau^{-1})^2}, \qquad (6)$$

where μ and τ^{-1} are inertial and relaxational parameters, respectively. Equation (6) allows for mixed inertial and relaxational dynamics and can estimate the acoustic phonon energy whether or not it is energetically well resolved from the elastic line. The main advantage of our multicomponent fit model, compared to models based on Lyddane-Sachs-Teller-type expressions [10], is that it does not assume any relationship between the LO and TO frequencies and the value of the dielectric function.

The various spectral components were summed, multiplied by a Bose factor, and fit to the experimental data. This removes the effects of thermal occupations of the various excitations, enabling a more meaningful comparison between spectra at different temperatures. The fit parameters can therefore be considered to represent the susceptibility, $\chi_s''(q, \omega)$, rather than the correlation function, $S_s(q, \omega)$ [Eq. (5)].

The full LO phonon dispersions for $x = 1.4\%$ are summarized in Fig. 4(d). In contrast to RPA predictions (Fig. 1), none of the phonons exhibit any observable shift with q. Rather, they remain near their bare frequencies at all momenta.

The momentum dependence of the plasmon for the $x = 1.4\%$ sample at $T = 300$ K, over the range $0 < q < 1.0$ r.l.u., is summarized in Fig. 5(d). The intensity of the plasmon was found to be highly q dependent: its integrated spectral weight grows monotonically with q, reaching a maximum at
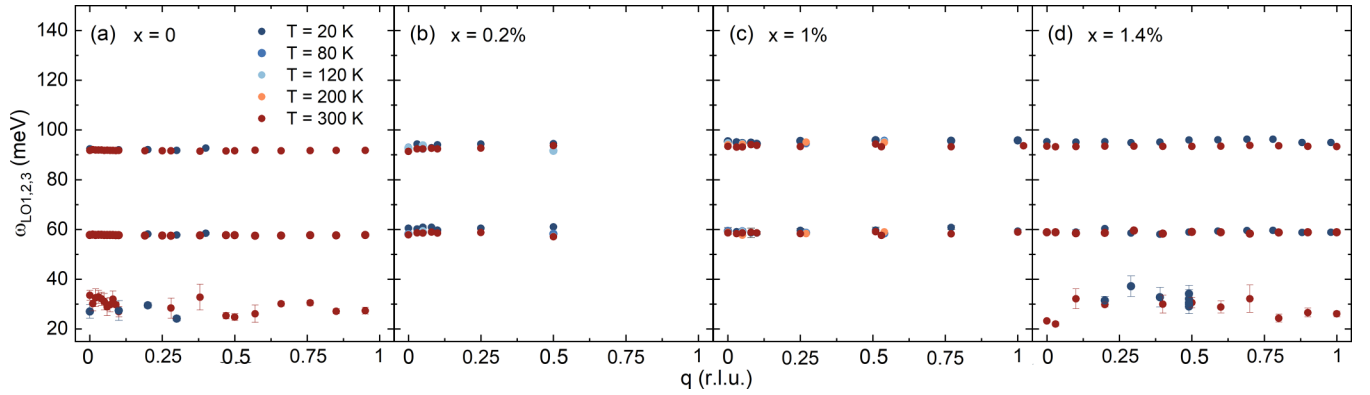
FIG. 4. LO phonon frequencies obtained from Fano fits at each q for different temperatures in the (a) $x = 0\%$, (b)$x = 0.2\%$, (c) $x = 1\%$, and (d) $x = 1.4\%$ samples. None of the LO phonons were found to shift as a function of q, in contrast to RPA predictions. There is little change in phonon frequency as a function of temperature. All points contain error bars, the LO2 and LO3 having values which are $\mathcal{O}(0.1\ \text{meV})$ and not visible on the scale of the plot. The LO1 phonon was not well resolved from the background and elastic line in the $x = 0.2\%$ and 1% samples, so was omitted from the fitting scheme for these compositions.

$q = 0.5$ r.l.u. For higher momenta, the plasmon intensity then falls again, reaching another minimum at $q = 1.0$ r.l.u., where the spectrum matches that at $q = 0$ due to the periodicity of reciprocal space.

Intriguingly, we found the fit value of the plasma frequency, shown as open circles in Fig. 5(d), to be independent of q, having the value $\omega_p = 93.1 \pm 5.3$ meV at all momenta. The statistical variation in the peak position is small compared to its full width at half maximum, $\Delta\omega_p = 119.4 \pm 6.2$ meV. We see no evidence for the q^2 dispersion or decay into the particle-hole continuum predicted by RPA (Fig. 1).

We now examine the temperature dependence of the various spectral features. For this sample with $x = 1.4\%$, as shown in Fig. 2(b), there is no measurable change to the

dispersion of the acoustic phonon between $T = 300$ and 20 K. The energy of the LO3 FK phonon was found to increase slightly from 93.4 ± 0.1 meV at $T = 300$ K to 95.5 ± 0.6 meV at $T = 20$ K [Figs. 4(d) and 6(a)]. However, no statistically significant shift to the LO1 or LO2 mode was observed.

The temperature dependence of the plasmon, however, is striking. This can be seen by comparing Fig. 5(d) to Fig. 5(h), the latter showing the full q dependence of the plasmon at $T = 20$ K. A clear reorganization of spectral weight indicates an increase of the plasma frequency from $\omega_p = 93.1 \pm 5.3$ meV at 300 K to $\omega_p = 142.5 \pm 10.2$ meV at 20 K. This dramatic change with temperature was previously observed in multiple IR optics experiments [10–12]. What we have shown here is
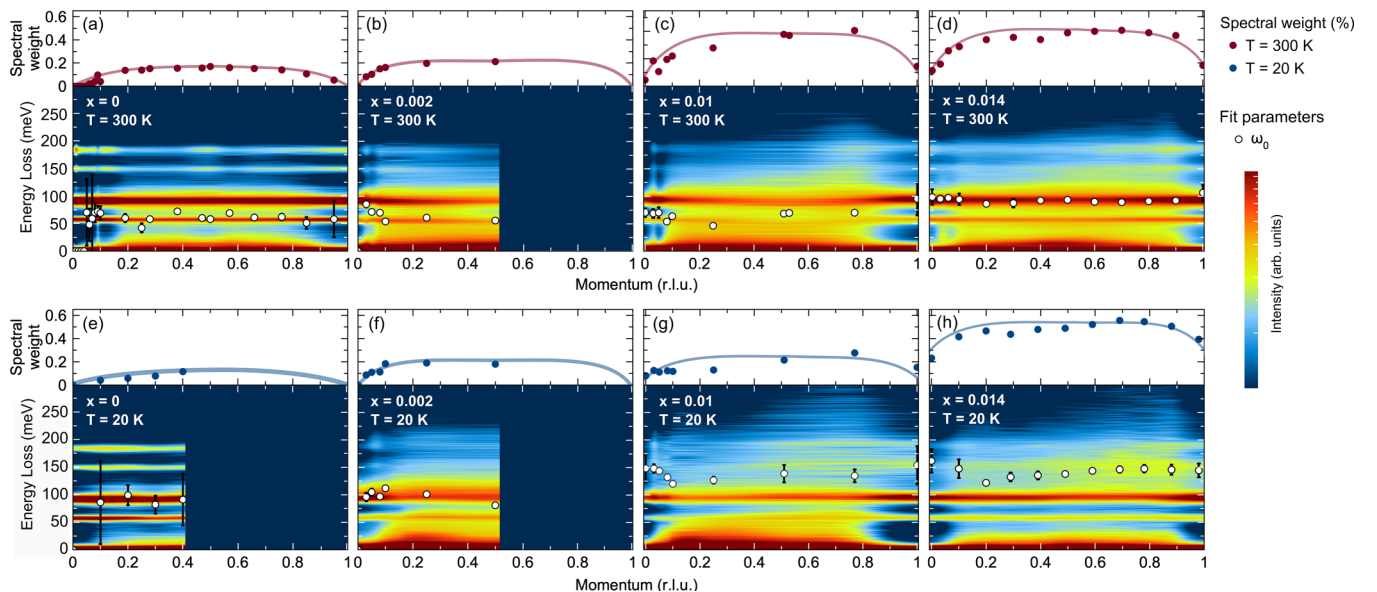

FIG. 5. Full M-EELS data sets taken at $T = 300$ K for the (a) $x = 0$, (b) $x = 0.2\%$, (c) $x = 1\%$, and (d) $x = 1.4\%$ samples and at 20 K for (e) $x = 0$, (f) $x = 0.2\%$, (g) $x = 1\%$, and (h) $x = 1.4\%$. The overlaid points show the peak position of the plasmon, ω_p, at each momentum, temperature, and composition. The plasma frequency increases with increased doping and with decreased temperature. The plots above each panel show the integrated intensity of the plasmon normalized by the total spectral weight. The solid curves are a guide to the eye.
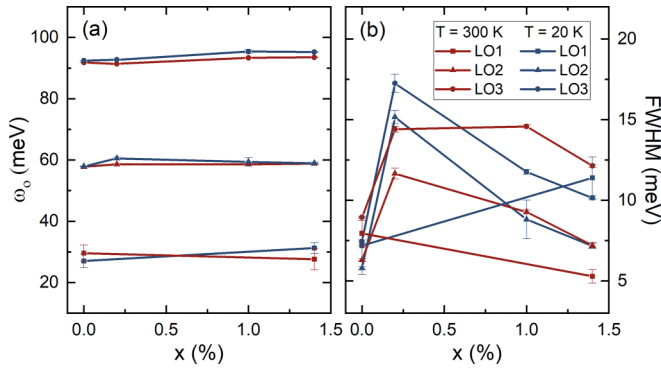
FIG. 6. LO phonon parameters as a function of doping. (a) Fit values of the phonon frequencies as a function of doping at $T = 20$ and 300 K. The values shown have been averaged over all q, the error bars representing the standard deviation. (b) Full width at half maximum linewidths of the LO1, LO2, and LO3 phonons at $q = 0$ for $T = 20$ and 300 K. The width of all modes is nonmonotonic in x, reaching a maximum value at $x = 0.2\%$.

that this shift takes place everywhere in the Brillouin zone, from $q = 0$ to the Brillouin zone boundary, $q = 0.5$ r.l.u.

Finally, we examine how these excitations evolve as the doping level, x, is changed. The dispersion of the acoustic phonon showed no discernible dependence on the doping level [Figs. 2(b), 3(b), 3(d), 3(f), and 3(h)]. The shape of the dispersion curve and maximum energy was the same in all compositions studied.

The LO phonon frequencies were found to shift with doping, as expected. However, not all LO frequencies increased monotonically with x, and the shifts were smaller than predicted by RPA. The fit values of the phonon frequencies are summarized in Figs. 4 and 6, as well as Table I. Comparing the undoped and highest doped samples at 300 K, the LO2 and LO3 phonons increase by 1.0 ± 0.11 meV and 1.7 ± 0.11 meV, respectively. At $T = 20$ K, the LO2 and LO3 phonons shift by 1.0 ± 0.46 meV and 2.8 ± 0.15 meV, respectively. These shifts are somewhat smaller than predicted by RPA (Fig. 1), though agree well with previous IR and surface EELS measurements at $q = 0$ [10,16,30,31]. Note that the intensity of the LO1 phonon was low compared to the other excitations, so our fits did not provide a highly constrained value for its frequency (in fact, it was not possible to fit the LO1 mode at all at $x = 0.2\%$ and $x = 1\%$, where it was left out of the fits altogether).

The phonon linewidths also showed a nonmonotonic dependence on x. In the $x = 0.2\%$ sample at $T = 300$ K and $q = 0$ r.l.u. [Fig. 3(c)], the phonons are significantly broader than at the other compositions. In particular, the width of the 93-meV LO3 phonon for $x = 0.2\%$ is a factor of 2.12 larger than at $x = 0$ [Fig. 6(b)]. The phonons sharpen again as doping is further increased to $x = 1\%$ and $x = 1.4\%$, though are never as sharp as in the $x = 0$ sample [Fig. 6(b)].

Despite its other anomalous properties, the doping dependence of the plasmon is rather conventional. The plasmon was observed in all four compositions studied, including the insulator, $x = 0$. The presence of a plasmon in insulating SrTiO$_3$ might be attributed to surface doping due to exposure to the electron beam, which could create oxygen vacancies [25], though other interpretations are possible (see Discussion). Nevertheless, as shown in Fig. 7(a), the plasma frequency, ω_p, is roughly linear in $\sqrt{n}$, n being the carrier density measured by Hall effect. Note, however, that $\omega_p(n)$ does not extrapolate to zero as $n \to 0$.

The other anomalous properties of the plasmon persist at all doping levels. Using the same Drude fit function, the fit value of the plasma frequency is highly temperature dependent [Fig. 7(b)], increasing by a factor 1.46, 1.49, 2.05, and 1.53 when cooling from 300 to 20 K, for the $x = 0$, 0.2%, 1%, and 1.4% samples, respectively (see also Fig. 5). The plasmon line shape is anomalously broad, and its frequency and width are independent of q (Fig. 5) at all compositions.

In all samples, except the $x = 1.4\%$ sample, the intensity of the background decreases as temperature is lowered (Fig. 5). In the highest doped sample, $x = 1.4\%$, this trend is reversed, with the plasmon intensity slightly increasing as the temperature is reduced from $T = 300$ K to $T = 20$ K. This increase suggests an enhancement of the susceptibility, $\chi''(q, \omega)$, at low temperature at this composition.

V. DISCUSSION

Overall, our surface M-EELS observations agree well with previous spectroscopic studies of the collective excitations of SrTi$_{1-x}$Nb$_x$O$_3$. The dispersion of the acoustic phonon is consistent with previous neutron-scattering measurements [27–29]. Our observation that the LO phonons shift very little with doping at $q = 0$ agrees with past IR studies reporting the same [10,16]. The energy of the plasmon, as well as its dramatic temperature dependence, also agree well with IR measurements (Fig. 7) [10,12]. The only discrepancy in

TABLE I. LO phonon frequencies at each doping at $T = 300$ K and $T = 20$ K. To account for greater fitting uncertainty, the LO1 phonon frequencies represent the average across the Brillouin zone with the error being the standard deviation. The LO2 and LO3 phonon frequencies and errors reflect the $q = 0$ peak position and error from fitting.

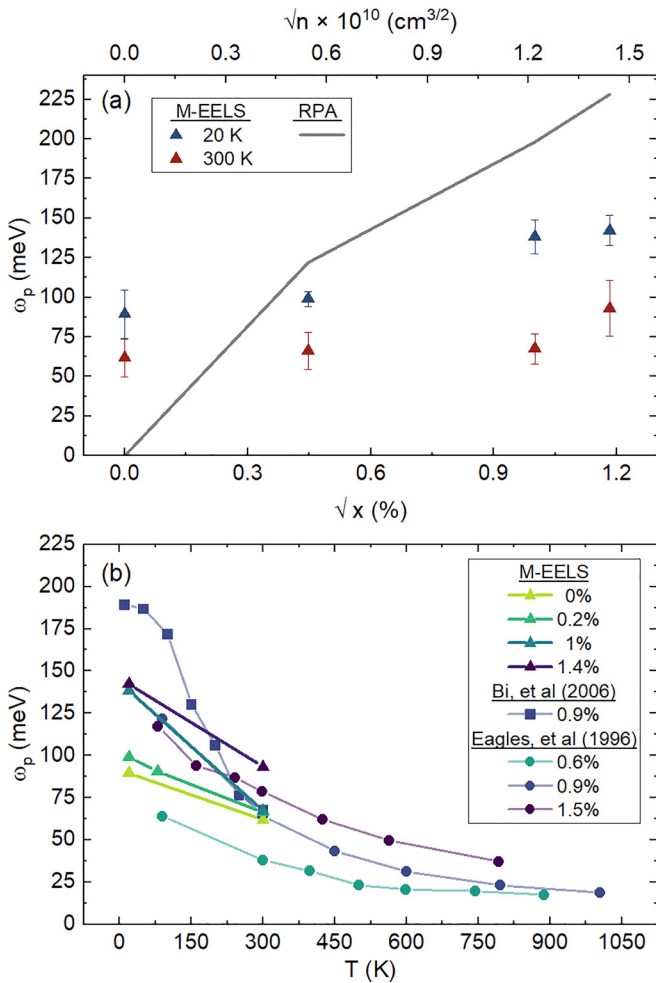|	$T = 300$ K				$T = 20$ K		
x (%)	LO1 (meV)	LO2 (meV)	LO3 (meV)	x (%)	LO1 (meV)	LO2 (meV)	LO3 (meV)
0	29.6 ± 2.66	57.8 ± 0.04	91.8 ± 0.03	0	27.0 ± 2.19	57.9 ± 0.06	92.4 ± 0.03
0.2		58.6 ± 0.28	91.4 ± 0.06	0.2		60.5 ± 0.4	92.7 ± 0.09
1		58.6 ± 0.09	93.4 ± 0.04	1		59.4 ± 1.3	95.4 ± 0.63
1.4	27.6 ± 3.45	58.8 ± 0.07	93.5 ± 0.08	1.4	31.3 ± 1.76	58.9 ± 0.4	95.2 ± 0.12

FIG. 7. Fit value of the plasma frequency, ω_p, averaged over all q, for different temperatures and compositions. (a) Plasma frequency as a function of $\sqrt{x}$ (bottom)/$\sqrt{n}$ (top) for $T = 20$ and 300 K. Error bars represent the standard deviation of ω_p across different momenta q. The solid line represents the value of the phonon-coupled plasmon at $q = 0$ from RPA. (b) Same data as panel (a), now plotted against temperature (filled triangles). Data from Ref. [12] (filled squares) and Ref. [11] (filled circles) have been added to this panel for comparison.

the literature is in the width of the plasmon. For doping value $x = 0.9\%$, Ref. [10] reported a FWHM $\Delta\omega_p = 59.5$ meV at $T = 300$ K, while Ref. [12] reported $\Delta\omega_p = 642$ meV under the same conditions. Our M-EELS measurements, shown in Fig. 3, give a number in between, $\Delta\omega_p = 130.4$ meV. Some of these differences may be due to different fit functions used to quantify the peak. Nevertheless, the good overall consistency between M-EELS and previous studies supports the validity of our results.

Comparison between our data and expectations from RPA are, however, less favorable. The optical phonons exhibit no measurable shift with q, appearing at the same frequency for both $q < k_F$ and $q > k_F$. Combined with the observation that LO phonons also do not shift appreciably with doping, our results suggest that screening simply does not affect the LO phonons in SrTi$_{1-x}$Nb$_x$O$_3$ in the way expected from RPA.

Nevertheless, doping has a strong effect on the phonon widths. The 16-meV linewidth of the LO3 phonon at $x = 0.2\%$, for example, is more than double its 5 meV width at $x = 0$. This is unlikely to be due to inhomogeneous broadening, since the total shift of the LO3 mode over the whole doping range investigated is only 1.7 meV. The width is therefore likely a real lifetime effect.

The extremely broad plasmon linewidth at $q = 0$, already reported in IR measurements [10,12], strongly contradicts the RPA prediction that it should have an infinite lifetime. Further, the plasmon does not exhibit the expected q^2 dispersion or decay into the particle-hole continuum (Fig. 1). This is unlikely to be due to poor surface quality or poor momentum resolution, since the dispersion of other excitations, notably the acoustic phonon, is pronounced (Fig. 2). The main finding of our study is that the dramatic temperature shift of the plasmon, observed previously at $q = 0$ in IR measurements, takes place everywhere in the Brillouin zone, from $q = 0$ to the zone boundary, $q = 0.5$ r.l.u.

Our results present a challenge to theory. In the simplest model of a doped semiconductor with a Fröhlich electron-phonon coupling, one would expect the dielectric function to exhibit identifiable, coupled phonon-plasmon modes that become overdamped only at momenta higher than the electron-hole continuum, as shown in Fig. 1 [18,33,34]. Such plasmon-phonon interference effects have been observed in other, similar materials, such as CdS and GaN [33,34]. In the case of SrTi$_{1-x}$Nb$_x$O$_3$, the plasmon is nondispersive and never long-lived. Our measurements therefore reveal a decidedly less "conventional" electronic state, and indicate that beyond-RPA techniques are required to explain the behavior of SrTi$_{1-x}$Nb$_x$O$_3$.

One speculative interpretation might be that the plasmon mixes more strongly with the anharmonic continuum *between* the LO phonons in SrTi$_{1-x}$Nb$_x$O$_3$, rather than with the phonons themselves. Note that the intensity of the plasmon increases rapidly with q (Fig. 5). This suggests the plasmon has significant lattice character, since scattering from lattice excitations $\sim(\mathbf{q} \cdot \mathbf{u})^2$, where $\mathbf{u}$ is the displacement vector of an atom.

Further, the line shape of the plasmon (Fig. 3), which resides beneath and between the LO phonons, has the qualitative appearance of a multiphonon continuum, which is present in all materials because of lattice anharmonicity [35–39]. This effect arises from scattering involving two or more phonons in the final state, which is allowed in the presence of phonon-phonon interactions. It appears as a continuum in spectroscopy experiments because the momentum of the individual phonons in the final state is not constrained. Its line shape, then, resembles the momentum-integrated density of states. A multiphonon continuum should be unpolarized, having mixed longitudinal and transverse character, and by symmetry can mix with a longitudinal plasmon. We conjecture that, rather than forming a distinct plasmon, the collective response of the doped electrons in SrTi$_{1-x}$Nb$_x$O$_3$ gets bound up in this multiphonon continuum because of the strong polaronic character of this material.

While somewhat speculative, this explanation could explain why the plasmon in SrTi$_{1-x}$Nb$_x$O$_3$ is dispersionless. The multiphonon line shape is already momentum integrated,

and would therefore have the same shape at all q, the only q dependence occurring in its intensity.

Further, the dramatic temperature dependence of ω_p might be understood in terms of lattice anharmonicity. In the presence of phonon-phonon interactions, the phonon self-energy depends on how many other phonons are present in the system. The center energy of this composite excitation might then shift with temperature because of phonon self-energy effects.

Finally, while we cannot rule out the presence of surface doping, this picture would also explain why the plasmon is visible in the insulator, $SrTiO_3$, in which the excitation could be understood to be a pure anharmonic continuum, without any plasmon character. As electrons are added through Nb doping, and this continuum acquired a plasmon character, its center frequency would shift $\sim \sqrt{n}$, though it would extrapolate to a nonzero energy as $n \rightarrow 0$, as we observe in Fig. 7.

Of course, the reason why the mixing would occur in this way is an open question. Jahn-Teller effects may be playing a role. Doping electrons into $SrTiO_3$ transforms a small number of the Ti^{4+} sites into Ti^{3+}, which in a cubic crystal field is an orbitally degenerate, Jahn-Teller ion, enhancing electron-phonon interactions and polaronic effects. Whatever the mechanism, it seems likely that investigating anharmonicity and the strong coupling between different collective excitations, may be needed to understand the plasmon in $SrTi_{1-x}Nb_xO_3$.

Additional insight on the nature of the plasmon in $SrTi_{1-x}Nb_xO_3$ might be obtained through two-dimensional optical spectroscopy [40]. Such methods have been successful in disentangling vibrational modes in molecular systems [41]. Such measurements on $SrTi_{1-x}Nb_xO_3$ using IR and terahertz radiation could reveal coupling between different modes, discriminate between homogeneous and inhomogeneous broadening, and reveal the fundamental relaxation and decoherence lifetimes of collective excitations [42–48].

[1] K. A. Müller and H. Burkard, SrTiO₃: An intrinsic quantum paraelectric below 4 K, Phys. Rev. B **19**, 3593 (1979).

[2] C. Collignon, X. Lin, C. W. Rischau, B. B. Fauqué, and K. Behnia, Metallicity and superconductivity in doped strontium titanate, Annu. Rev. Condens. Matter Phys. **10**, 25 (2019).

[3] Y. Takada, Theory of superconductivity in polar semiconductors and its application to *n*-type semiconducting SrTiO₃, J. Phys. Soc. Jpn. **49**, 1267 (1980).

[4] J. Ruhman and P. A. Lee, Superconductivity at very low density: The case of strontium titanate, Phys. Rev. B **94**, 224515 (2016).

[5] L. P. Gor'kov, Back to mechanisms of superconductivity in low-doped strontium titanate, J. Supercond. Nov. Magn. **30**, 845 (2017).

[6] V. J. Emery and S. A. Kivelson, Superconductivity in bad metals, Phys. Rev. Lett. **74**, 3253 (1995).

[7] J. M. Edge, Y. Kedem, U. Aschauer, N. A. Spaldin, and A. V. Balatsky, Quantum critical origin of the superconducting dome in SrTiO₃, Phys. Rev. Lett. **115**, 247002 (2015).

[8] J. G. Bednorz and K. A. Müller, Perovskite-type oxides—The new approach to high-T_c superconductivity, Rev. Mod. Phys. **60**, 585 (1988).

[9] X. Lin, C. W. Rischau, L. Buchauer, A. Jaoui, B. Fauqué, and K. Behnia, Metallicity without quasi-particles in room-temperature strontium titanate, npj Quantum Mater. **2**, 1 (2017).

[10] F. Gervais, J. L. Servoin, A. Baratoff, J. G. Bednorz, and G. Binnig, Temperature dependence of plasmons in Nb-doped SrTiO₃, Phys. Rev. B **47**, 8187 (1993).

[11] D. M. Eagles, M. Georgiev, and P. C. Petrova, Explanation for the temperature dependence of plasma frequencies in using mixed-polaron theory, Phys. Rev. B **54**, 22 (1996).

[12] C. Z. Bi, J. Y. Ma, J. Yan, X. Fang, B. R. Zhao, D. Z. Yao, and X. G. Qiu, Electron-phonon coupling in Nb-doped SrTiO₃ single crystal, J. Phys.: Condens. Matter **18**, 2553 (2006).

[13] D. van der Marel, J. L. M. van Mechelen, and I. I. Mazin, Common Fermi-liquid origin of T^2 resistivity and superconductivity in *n*-type SrTiO₃, Phys. Rev. B **84**, 205111 (2011).

[14] C. Collignon, P. Bourges, B. Fauqué, and K. Behnia, Heavy nondegenerate electrons in doped strontium titanate, Phys. Rev. X **10**, 031025 (2020).

[15] J. L. M. van Mechelen, D. van der Marel, C. Grimaldi, A. B. Kuzmenko, N. P. Armitage, N. Reyren, H. Hagemann, and I. I. Mazin, Electron-phonon interaction and charge carrier mass enhancement in SrTiO₃, Phys. Rev. Lett. **100**, 226403 (2008).

[16] J. T. Devreese, S. N. Klimin, J. L. M. van Mechelen, and D. van der Marel, Many-body large polaron optical conductivity in $SrTi_{1-x}Nb_xO_3$, Phys. Rev. B **81**, 125119 (2010).

[17] M. Dressel and G. Grüner, *Electrodynamics of Solids: Optical Properties of Electrons in Matter* (Cambridge University Press, Cambridge, UK, 2002).

[18] A. S. Barker, *Colloquium on the Optical Properties and Electronic Structure of Metals and Alloys*, edited by F. Abeles (North-Holland Pub. Co., 1966).

[19] G. D. Mahan, *Many-Particle Physics*, Physics of Solids and Liquids (Springer, New York, 2000).

[20] X. Lin, B. Fauqué, and K. Behnia, Scalable T^2 resistivity in a small single-component Fermi surface, Science **349**, 945 (2015).

[21] S. Vig, A. Kogar, M. Mitrano, A. A. Husain, L. Venema, M. S. Rak, V. Mishra, P. D. Johnson, G. D. Gu, E. Fradkin, M. R. Norman, and P. Abbamonte, Measurement of the dynamic charge response of materials using low-energy,

momentum-resolved electron energy-loss spectroscopy (M-EELS), SciPost Phys. **3**, 026 (2017).

[22] A. Kogar, S. Vig, Y. Gan, and P. Abbamonte, Temperature-resolution anomalies in the reconstruction of time dynamics from energy-loss experiments, J. Phys. B: At., Mol. Opt. Phys. **47**, 124034 (2014).

[23] A. A. Husain, E. W. Huang, M. Mitrano, M. S. Rak, S. I. Rubeck, X. Guo, H. Yang, C. Sow, Y. Maeno, B. Uchoa, T. C. Chiang, P. E. Batson, P. W. Phillip, and P. Abbamonte, Pines' demon observed as a 3D acoustic plasmon in Sr_2RuO_4, Nature (London) **621**, 66 (2023).

[24] J. Chen, X. Guo, C. Boyd, S. Bettler, C. S. Kengle, D. Chaudhuri, F. Hoveyda, A. Husain, J. Schneeloch, G. Gu, P. Phillips, B. Uchoa, T.-C. Chiang, and P. Abbamonte, Plasmons and long-wavelength density fluctuations in the strange metal $Bi_2Sr_2CaCu_2O_{8+x}$, arXiv:2306.03681.

[25] W. Meevasana, P. D. C. King, R. H. He, S.-K. Mo, M. Hashimoto, A. Tamai, P. Songsiriritthigul, F. Baumberger, and Z.-X. Shen, Creation and control of a two-dimensional electron liquid at the bare $SrTiO_3$ surface, Nat. Mater. **10**, 114 (2011).

[26] I. S. Sokolovi'c, M. Schmid, U. Diebold, and M. Setvin, Incipient ferroelectricity: A route towards bulk-terminated $SrTiO_3$, Phys. Rev. Mater. **3**, 034407 (2019).

[27] G. Shirane and Y. Yamada, Lattice-dynamical study of the 110 K phase transition in $SrTiO_3$, Phys. Rev. **177**, 858 (1969).

[28] N. Choudhury, E. J. Walter, A. I. Kolesnikov, and C.-K. Loong, Large phonon band gap in $SrTiO_3$ and the vibrational signatures of ferroelectricity in $A TiO_3$ perovskites: First-principles lattice dynamics and inelastic neutron scattering, Phys. Rev. B **77**, 134111 (2008).

[29] X. He, D. Bansal, B. Winn, S. Chi, L. Boatner, and O. Delaire, Anharmonic eigenvectors and acoustic phonon disappearance in quantum paraelectric $SrTiO_3$, Phys. Rev. Lett. **124**, 145901 (2020).

[30] A. Baden, P. Cox, R. Egdell, A. Orchard, and R. Willmer, Observation of surface optical phonons on $SrTiO_3$ (100), J. Phys. C: Solid State Phys. **14**, L1081 (1981).

[31] F. Li and G. A. Sawatzky, Electron phonon coupling versus photoelectron energy loss at the origin of replica bands in photoemission of fese on $SrTiO_3$, Phys. Rev. Lett. **120**, 237001 (2018).

[32] P. M. Chaikin and T. C. Lubensky, *Principles of Condensed Matter Physics* (Cambridge University Press, Cambridge, 1995).

[33] J. F. Scott, T. C. Damen, J. Ruvalds, and A. Zawadowski, Plasmon-phonon interference in CdS, Phys. Rev. B **3**, 1295 (1971).

[34] A. Dyson, Phonon–plasmon coupled modes in GaN, J. Phys.: Condens. Matter **21**, 174204 (2009).

[35] R. A. Cowley and A. D. B. Woods, Inelastic scattering of thermal neutrons from liquid helium, Can. J. Phys. **49**, 177 (1971).

[36] A. Miller, D. Pines, and P. Nozières, Elementary excitations in liquid helium, Phys. Rev. **127**, 1452 (1962).

[37] W. Stirling, Multiphonon scattering from superfluid ^{4}Helium, Phys. B: Condens. Matter **165-166**, 501 (1990).

[38] K. H. Andersen, W. G. Stirling, R. Scherm, A. Stunault, B. Fak, H. Godfrin, and A. J. Dianoux, Collective excitations in liquid ^{4}He: I. Experiment and presentation of data, J. Phys.: Condens. Matter **6**, 821 (1994).

[39] N. W. Ashcroft and N. D. Mermin, *Solid State Physics* (Holt-Saunders, 1976).

[40] S. Mukamel, *Principles of Nonlinear Optical Spectroscopy* (Oxford University Press, New York, 1995).

[41] S. T. Cundiff and S. Mukamel, Optical multidimensional coherent spectroscopy, Phys. Today **66** (7), 44 (2013).

[42] Y. Wan and N. P. Armitage, Resolving continua of fractional excitations by spinon echo in THz 2D coherent spectroscopy, Phys. Rev. Lett. **122**, 257401 (2019).

[43] W. Choi, K. H. Lee, and Y. B. Kim, Theory of two-dimensional nonlinear spectroscopy for the kitaev spin liquid, Phys. Rev. Lett. **124**, 117205 (2020).

[44] Z.-L. Li, M. Oshikawa, and Y. Wan, Photon echo from lensing of fractional excitations in tomonaga-luttinger spin liquid, Phys. Rev. X **11**, 031035 (2021).

[45] F. Gerken, T. Posske, S. Mukamel, and M. Thorwart, Unique signatures of topological phases in two-dimensional THz spectroscopy, Phys. Rev. Lett. **129**, 017401 (2022).

[46] J. Lu, Y. Zhang, H. Y. Hwang, B. K. Ofori-Okai, S. Fleischer, and K. A. Nelson, Nonlinear two-dimensional terahertz photon echo and rotational spectroscopy in the gas phase, Proc. Natl. Acad. Sci. USA **113**, 11800 (2016).

[47] J. Lu, X. Li, H. Y. Hwang, B. K. Ofori-Okai, T. Kurihara, T. Suemoto, and K. A. Nelson, Coherent two-dimensional terahertz magnetic resonance spectroscopy of collective spin waves, Phys. Rev. Lett. **118**, 207204 (2017).

[48] F. Mahmood, D. Chaudhuri, S. Gopalakrishnan, R. Nandkishore, and N. P. Armitage, Observation of a marginal Fermi glass, Nat. Phys. **17**, 627 (2021).